

Solution-Processed Two-Dimensional Ultrathin InSe Nanosheets

Jannika Lauth,^{*,†,‡,§} Friederike E. S. Gorris,^{†,‡} Mahdi Samadi Khoshkhoo,[‡] Thomas Chassé,[‡] Wiebke Friedrich,[‡] Vera Lebedeva,[‡] Andreas Meyer,[‡] Christian Klinke,[‡] Andreas Kornowski,[‡] Marcus Scheele,[‡] and Horst Weller[‡]

[‡]Institute of Physical Chemistry, University of Hamburg, Grindelallee 117, D-20146 Hamburg, Germany

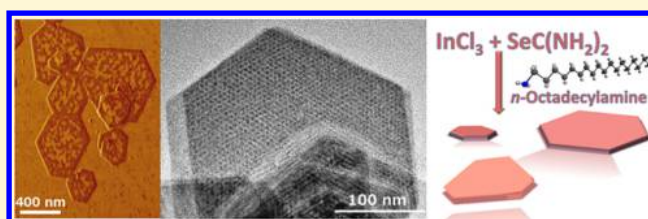
[§]Chemical Engineering Department, Delft University of Technology, Julianalaan 136, NL-2628 BL Delft, The Netherlands

[†]Institute for Physical and Theoretical Chemistry, Eberhard Karls University, Auf der Morgenstelle 18, D-72076 Tuebingen, Germany

Supporting Information

ABSTRACT: The rise of two-dimensional (2D) graphene-cognated crystals with nonzero band gaps like transition metal dichalcogenides has led to a rapidly increasing interest in their dimensionality-dependent anisotropic properties, which bear high potential for ultrathin electronics. 2D crystals of the III–VI metal chalcogenide InSe represent a new kind of material class predestined for the use in optoelectronic applications as highly responsive photodetectors and field-effect transistors.

We present a solution-processable method for 2D ultrathin InSe nanosheets (≤ 5 nm with ligands, lateral sizes up to ~ 800 μm) with a detailed characterization of the sheet formation by a lamellar ligand templated growth. Optical and electrical transport properties, as well as in depth analysis of the crystal structure and stoichiometry of the colloidal nanosheets by electron and atomic force microscopy, X-ray photoelectron spectroscopy, and scattering methods complete this comprehensive study on a wet-chemical alternative to produce ultrathin InSe nanosheets.



INTRODUCTION

2D semiconductors with a band gap, like van der Waals layered transition metal dichalcogenides (e.g., MoS_2 , MoSe_2 , WS_2 , WSe_2) have come to fame as suitable materials to solve the zero band gap dilemma in graphene.¹ Drastic alterations in the electronic structure due to the lowered dimensionality have led to their successful implementation in thin film electronics such as photodetectors and field-effect transistors (FETs) in the past decade.^{2–9} For instance, the indirect band gap of bulk MoS_2 becomes direct for few-layered sheets. Among these well-known 2D semiconductors, one material recently moved into focus: exfoliated InSe, a van der Waals layered III–VI metal chalcogenide with an atomically smooth surface and high thermal stability up to 660 °C. It has recently proven its highly promising (opto)electronic properties as image sensor,¹⁰ high mobility FET (1×10^3 $\text{cm}^2/(\text{V s})$),^{11,12} and even outperformed other 2D crystal-based compounds like MoS_2 , GaS, and GaSe as high responsivity photodetector (spanning a broad spectral range of 450–785 nm).^{13–15} Ab initio studies forecast a semiconductor to metal transition in single InSe layers when an electric field is applied perpendicular to the layer.¹⁶ However, the valence electron mismatch in the indium selenide system generally complicates its synthesis and leads to the formation of different phases and crystal structures, as well as numerous stoichiometries of the material.^{17,18} One layer of InSe consists of 2 Se^{2-} anions and a $[\text{In}_2]^{4+}$ diatomic cation, which forms a weak internal In–In bond leading to the common 4-atomic Se–In–In–Se motif (see Figure 1b).^{19,20} 2D ultrathin InSe layers in the present study have a hexagonal crystal structure,

described by the lattice constants a (4.05 Å) and c (16.93 Å),¹⁹ exhibit the maximum of one unit cell in thickness (see Figure 1a).

When reducing layered InSe in thickness and thereby confining the material in the z -direction, an unusual direct-to-indirect band gap transition occurs as in contrast to other 2D semiconductors like MoS_2 (direct band gap in layers of atomic thickness).²¹ The reason for the favored indirect band gap transition in few-layered InSe originates from a reduced interlayer interaction, setting in when a crystal thickness of ~ 7 monolayers is reached. The reduced layer interaction lowers the intrinsically momentum forbidden indirect $\Gamma \rightarrow \text{M}$ transition of bulk InSe energetically slightly below the allowed direct $\Gamma \rightarrow \Gamma$ transition in 2D InSe.^{22,23}

A common way to produce few-layered 2D InSe involves exfoliation of thin layers from bulk InSe crystals.^{10,11,13–15,24,25} 2D In_2Se_3 layers are also grown via chemical vapor deposition and epitaxial growth.^{26–28} Although the exfoliation approach of InSe yields layers of considerable lateral dimensions (several 100 μm), the growth of the bulk InSe crystals requires tedious bulk InSe crystals growth with an exact $\text{In}_{1.04}\text{Se}_{0.96}$ ratio for the Bridgmann method¹⁸ proves to be rather inefficient for larger-scale dimensions and lacks the simplicity of wet-chemical methods.

Received: November 30, 2015

Revised: February 14, 2016

Published: February 21, 2016

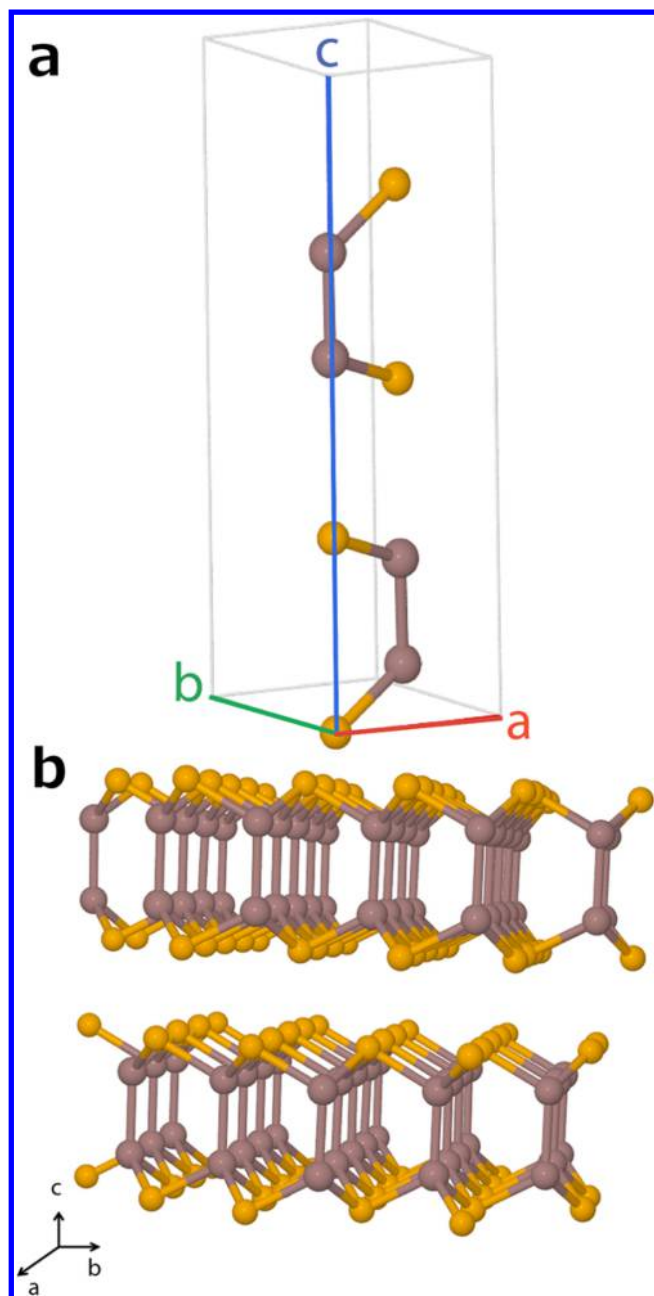


Figure 1. Hexagonal crystal structure of InSe with brown spheres referring to In and orange spheres referring to Se, (a) InSe hexagonal unit cell, (b) side view on the layered lattice structure with lattice constant c (16.93 Å),¹⁹ the maximum thickness of ultrathin InSe nanosheets.

Colloidal processing of 2D crystals offers a flexible alternative to exfoliation techniques, makes semiconductors available, which intrinsically lack van der Waals interaction²⁹ and has been significantly advanced by researchers in the past decade.^{30–35} Generally, two ways to describe 2D colloidal growth are widely accepted. One is the oriented attachment mechanism of very small nanocrystal (NC) nuclei by their high-energy surface sites, forming a 2D array.²⁹ This model has been extended by taking into account an additional mechanism for the formation: The combination of a hard core (PbS NCs) with a soft molecule (long-chain oleic acid ligand) in a mesoscale building block (under deviatoric stress)³⁶ yields 2D crystals stabilized by a “soft” ligand template. The second way to

describe 2D crystal growth has been initiated by Hyeon and co-workers. They were the first to describe the composition of a lamellar soft template yielding ultrathin CdSe nanosheets by the formation of $\text{CdCl}_2(\text{amine})_2$ complexes from the precursor and the solvent/ligand.^{33,34,37} Buhro and co-workers advanced the mesophase template approach by evaluating the double-lamellar structure formed by primary amines, which stabilizes $(\text{CdSe})_{13^-}$ and $(\text{CdSe})_{34^-}$, as well as other II–VI magic size nanoclusters as synthons for 2D nanocrystals.^{30,38–41} They have recently proven the validity of the mesophase template approach for the synthesis of PbS platelets with primary amines as templating ligands.⁴² Although the ligand template approach yields numerous 2D semiconductors including CuS, ZnS, Bi_2S_3 , and Sb_2S_3 ,⁴³ there are only a few wet-chemical ways for 2D InSe, yielding rather small InSe nanosheets or instable reaction products.^{44,45}

We therefore present a facile solution-processable way for stable colloidal ultrathin InSe nanosheets with lateral dimensions up to ~ 800 nm by a lamellar ligand templated route. For the first time, the atomic thickness, crystal structure, and chemical composition of the hexagonal phase InSe layers are fully characterized by atomic force microscopy (AFM), electron diffraction (ED), and X-ray photoelectron spectroscopy (XPS). The crystalline inorganic–organic InSe–organic template structure is evaluated by grazing incidence small-angle X-ray scattering (GISAXS). Confocal absorption and photoluminescence measurements on ultrathin InSe layers reveal a strong size quantization in the z -direction, and electrical transport measurements on the sheets emphasize their potential for ultrathin optoelectronics.

EXPERIMENTAL SECTION

Chemicals. All chemicals were used as received without further purification. Indium(III) chloride (InCl_3 , anhydrous powder ($\geq 99.999\%$ trace metals basis)) and selenourea ($\text{SeC}(\text{NH}_2)_2$, 98%) were purchased from Sigma-Aldrich and stored under nitrogen in a glovebox. Octadecylamine (97%) and 1-octadecene (90%, technical grade), toluene (p.a.), and chloroform (p.a.) were acquired from Sigma-Aldrich and kept under ambient conditions. 2-Propanol (p.a.) was purchased from Merck.

InSe Nanosheet Synthesis. In a three-necked flask, (A) equipped with a thermocouple and septum, 18.2 mmol (4.9 g) octadecylamine are combined with 0.076 mmol (17 mg) indium(III) chloride inside a nitrogen filled glovebox. A second threenecked flask (B) is filled with 0.30 mmol (37 mg) of selenourea inside the glovebox. Both flasks are transferred to a Schlenk-line and set under nitrogen flow. Flask A is heated for 1 h under an oil pump vacuum to 75 °C to melt and degas ODA. Subsequently it is set under nitrogen, heated to 130 °C for 10 min (for stable mesophase formation) and afterward cooled to 100 °C for reaction. During heating of reaction flask A, 4.0 mL of 1-octadecene are added to flask B and the reaction solution is heated to 220 °C under nitrogen to start the formation of reactive selenium species from selenourea. After the selenium precursor reaction mixture is pale yellow, it is cooled to 120 °C, transferred by syringe and rapidly injected into flask A. The reaction mixture is heated to 240 °C for 1 h to react. The opaque brownish product is cooled to 50 °C after reaction and 5.0 mL of chloroform or toluene are added to prevent gelation of the mixture.

The crude product is purified by adding 5.0 mL of 2-propanol to the solution and centrifugation at 2000 g for 5 min. After discarding the colorless supernatant, the InSe nanosheets are redispersed in 3.0 mL of chloroform or toluene. This purification step is repeated two more times. InSe nanosheets for analysis and characterization are dispersed in 4 mL of chloroform or toluene.

Transmission Electron Microscopy (TEM). TEM imaging was conducted by using a JEOL JEM 2200FS (UHR) with CESCOR and

CETCOR corrector at an acceleration voltage of 200 kV or a JEOL JEM 1011 microscope at 100 kV.

Energy Dispersive X-ray Spectroscopy (EDS). Quantitative elemental analysis of InSe nanosheets was performed using a Si(Li) JEOL JED-2300 energy-dispersive X-ray detector equipped at the JEOL JEM 2200FS.

Scanning Electron Microscopy (SEM). SEM images were obtained on a LEO1550 scanning electron microscope with a spatial resolution of 1 nm.

Atomic Force Microscopy (AFM). AFM was conducted with a Veeco MultiMode microscope. Images were performed in tapping mode and processed for clarity with the image editing software Gwyddion 2.38.

Powder X-ray Diffraction (XRD). Powder XRD was recorded using a Philips X'Pert Diffractometer with Bragg–Brentano geometry on applying copper- $K\alpha$ radiation.

X-ray Photoelectron Spectroscopy (XPS). XPS measurements were carried out using a SPECS spectrometer equipped with a XRS0 X-ray source (Al K_{α} , working at 12.5 kV and 20 mA, 1486.61 eV) and a PHOIBOS 100 MCD analyzer. The pressure in the analyzer chamber was maintained below 5×10^{-10} mbar during the measurements. All survey spectra, scans of 1000 eV, were taken at analyzer pass energy of 50 eV. High-resolution scans were performed at the pass energy of 20 eV and steps of 0.05 eV. The binding energies were corrected for electrical charge effects by referencing to C 1s sp^3 peak, which was assumed to have a binding energy of 284.6 eV. The photoelectrons were detected at a takeoff angle of $\Phi = 0^\circ$ with respect to the surface normal. Acquisition and storage of data were accomplished using SpecsLab software version 2.35-r13657. Data were converted to VAMAS format and processed using Unifit2014 software. Data fitting was performed using Gauss-Lorentz profiles. The background was calculated and subtracted using the Shirley method. Each spectrum was also corrected for the satellite peaks ($\Delta = 9.8$ and 11.8 eV from $K_{\alpha 3}$ and $K_{\alpha 4}$, respectively). The sensitivity factors used for In($3d_{3/2}$), In($3d_{5/2}$), In($3d$), Se($3d_{3/2}$), Se($3d_{5/2}$), and Se($3d$) were 9.22, 13.32, 22.54, 0.934, 1.36, and 2.294, respectively.

Grazing Incidence Small-Angle X-ray Scattering (GISAXS). Scattering profiles/curves of InSe nanosheets were obtained with an Incoatec X-ray source $I\mu S$ with Quazar Montel optics at a wavelength of 0.154 nm, a focal spot size at the sample of 1 mm² and at an incidence angle of 0.3° . The distance between the sample and the CCD-Detector Rayonix SX165 was 1.6 m (measurement time per sample = 30 min). The revealed scattering patterns were radially integrated, transformed into GISAXS curves and analyzed and fitted with the software Scatter.^{46,47}

Absorption. Absorption measurements of the opaque and slightly turbid samples of the InSe nanosheets were performed in solution on a Cary 500 UV–vis–NIR (Varian) spectrometer equipped with an integrating sphere module.

Emission. Emission spectra of the InSe nanosheets were recorded with a spectrometer SpectraPro-300i from Acton Research using a CCD camera Imager QE from LaVision at an excitation wavelength of 470 nm. The diluted InSe sample was drop casted on a clean glass slide and point measurements with a 500 nm long-pass filter at higher PL intensity were performed.

Confocal Microscopy. The fluorescence intensity and transmission images of individual InSe nanosheets and sheet stacks were acquired with a setup consisting of a confocal laser scanning microscope (CLSM) FV 1000 (Olympus) coupled with a time-correlated single photon counting (TCSPC) unit (PicoQuant). A pulsed laser diode operating at 405 nm was used for excitation and PL was detected with an avalanche photodiode (APD) SPCM-AQR (PerkinElmer) by using a 500 nm long-pass filter.

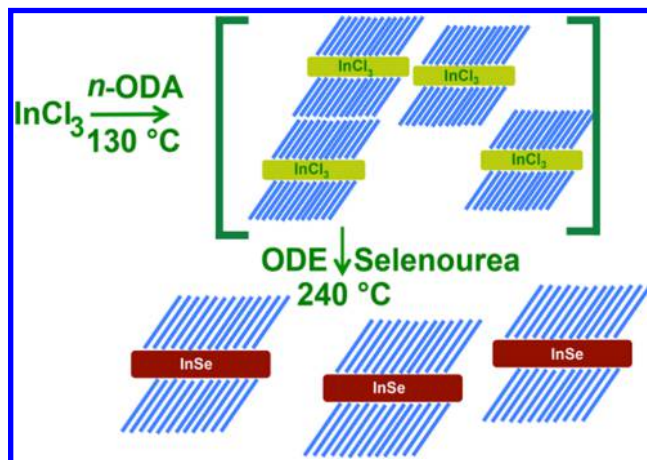
For correlating CLSM measurements with individual InSe nanosheets and sheet stacks tracked by SEM, a SiN grid with nine windows as substrate assured CLSM measurements at a retrievable sample section. Each sample section was scanned in transmission and PL mode. The diluted InSe nanosheet solution in chloroform was spin-coated onto the substrate with 4000 rpm. The substrate was centered on an object slide.

Electrical Transport Measurements. InSe nanosheets were drop-casted onto a highly n-doped silicon substrate with a 300 nm insulating layer of silicon oxide and gold contacts written by electron-lithography. After drop-casting, the samples were transferred to a probe station connected to a parameter analyzer, and electrical transport measurements were performed at room temperature under vacuum on a 4200-SCS semiconductor characterization system from Keithley Instruments inside a VFTTP4 probestation by Lake Shore Cryotronics.

RESULTS AND DISCUSSION

Colloidal InSe Nanosheet Synthesis. The indium precursor for reaction, indium(III) chloride, is mixed with

Scheme 1. InSe Nanosheets by Ligand Templated Growth with ODA^a



^aFormation of a lamellar ligand template from ODA with $InCl_3$ precedes the growth of ultrathin InSe layers. After transferring selenourea (dissolved/suspended in ODE) to the reaction, InSe nanosheets are obtained at $240^\circ C$.

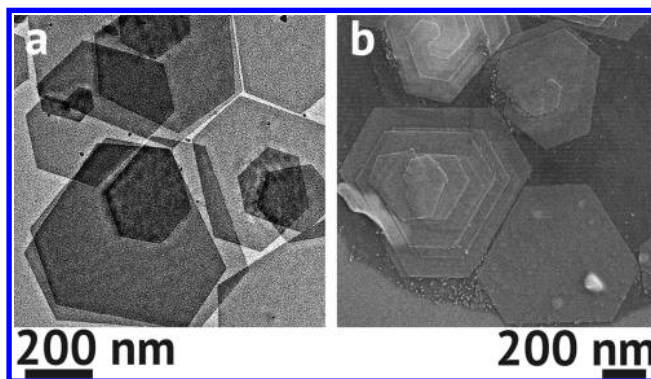


Figure 2. InSe nanosheets with (a) lateral sizes ranging from 350–800 nm (see also Figure S1), (b) multiple InSe sheet stacks.

octadecylamine (ODA) and gradually heated to $75^\circ C$ under an oilpump vacuum to melt and degas ODA. The temperature then is raised to $130^\circ C$ under nitrogen flow and held for 10 min to form an indium-ODA complex/mesophase (see Scheme 1), followed by cooling the reaction mixture to $100^\circ C$ to add the selenium precursor, selenourea ($SeC(NH_2)_2$) dissolved/suspended in 1-octadecene (ODE). ODA plays a major role as templating ligand for the formation of 2D InSe nanosheets, similar to the role of oleic acid during the crystallization of PbS nanosheets as described previously.²⁹ We note that Buhro and

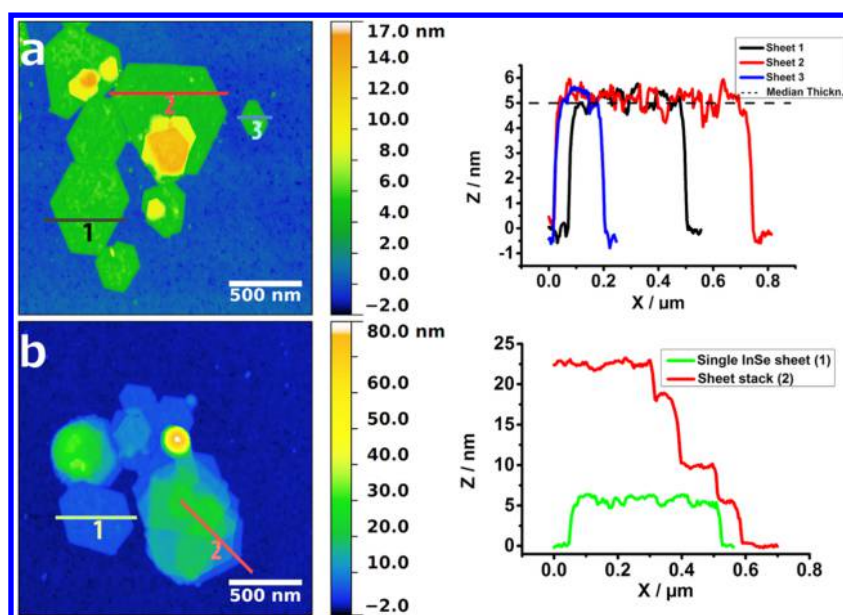


Figure 3. AFM images of single InSe nanosheets: (a) nanosheets with different lateral dimensions and median total thickness of 5 nm, (b) single InSe sheet in comparison with a four-layer sheet stack, repeatedly showing a layer thickness of ~ 5 nm and a stack height of ~ 22.5 nm.

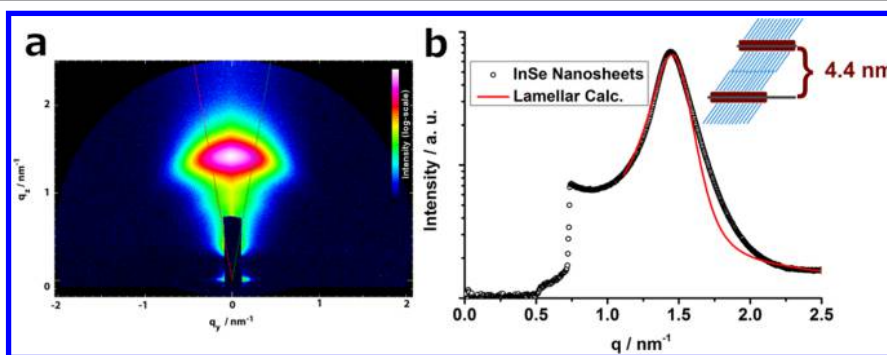


Figure 4. GISAXS curve of InSe sheets (a) 2D scattering pattern of InSe nanosheets lying flat on the surface with scattering in the q_z -direction and no long-range ordering in q_y -direction, area enclosed by the two lines resembles the data set used for the 1D projection in (b): 1D scattering pattern of InSe nanosheets in their lamellar ODA template, exhibiting a scattering periodicity of 4.4 nm (± 0.1 nm); assuming fully tilted ODA molecules of ~ 1.7 nm length per molecule yields an inorganic InSe layer thickness of ~ 1 nm (one InSe motif).

co-workers recently reported on the role of different primary amines as lamellar templates for the formation of ultrathin PbS nanosheets at low reaction temperatures.⁴² We believe a similar mechanism to be operative also in the present study. In our case, ODA acts as (assisting) template for the formation of InSe nanosheets at elevated temperatures (see Scheme 1). A 4-fold excess of selenourea is crucial to obtain the desired product. Experiments with an equimolar ratio of indium(III) chloride to selenourea yielded undefined crystalline InSe agglomerates, whereas more than a 4-fold selenourea excess for reaction yielded small particle-like assemblies. During reaction, $\text{SeC}(\text{NH}_2)_2$ undergoes decomposition at elevated temperatures, subsequently a vulcanization (similar to sulfur) with the double bond of ODE is assumed. This reaction, in which a reactive selenium species is released at higher temperatures to form cyclic octaselenium, chain-like selenium and short selenium bridges coordinating to the ODE double bond, has been described by Bullen et al.⁴⁸ In the presence of the templating effect of ODA, the reactive selenium species and the lamellar indium-ODA complex/mesophase yield InSe nanosheets at 240 °C (see Scheme 1).

Formation of a lamellar ligand template from ODA with InCl_3 precedes the growth of ultrathin InSe layers. After transferring selenourea (dissolved/suspended in ODE) to the reaction, InSe nanosheets are obtained at 240 °C.

Figure 2a depicts a typical TEM micrograph of ultrathin hexagonal InSe nanosheets after 60 min at 240 °C with lateral dimension of sheets ranging from 350–800 nm (Figure S1 for additional TEM and SEM micrographs). The SEM image in Figure 2b shows characteristic stacks of multiple InSe sheets. A small part of the InSe nanosheets exhibit a screw-dislocated structure, presumably caused by stacking faults, which are known to occur during the growth of InSe.¹⁹

Besides the mentioned reaction conditions, the reaction time has a strong influence on the size, lateral dimension and stability of the InSe nanosheets. Sampling at different reaction times shows the formation of smaller sheets with sizes of ~ 250 nm after 5 min at 240 °C. InSe nanosheet samples after 5 min of reaction lack the long time stability of their 60 min reaction counterparts under ambient conditions. Upon further progress of reaction, InSe layers grow to reach their full size between 30–60 min of reaction (Figure 2). After 180 min at 240 °C, InSe nanosheets start to disintegrate, yielding undefined InSe

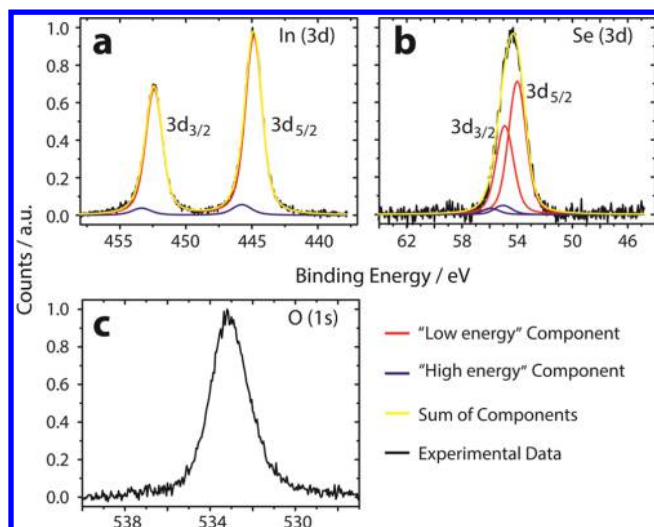


Figure 5. XPS of InSe nanosheets in (a) the In(3d) core level, (b) the Se(3d) core level, and (c) the O(1s) core level region. Two components for In and Se are detected, the attribution and fitting parameters of which are detailed in the main text. The O(1s) signal is not fitted because of a likely contribution from various unspecific contaminants such as surface oxygen, alcohols, etc.

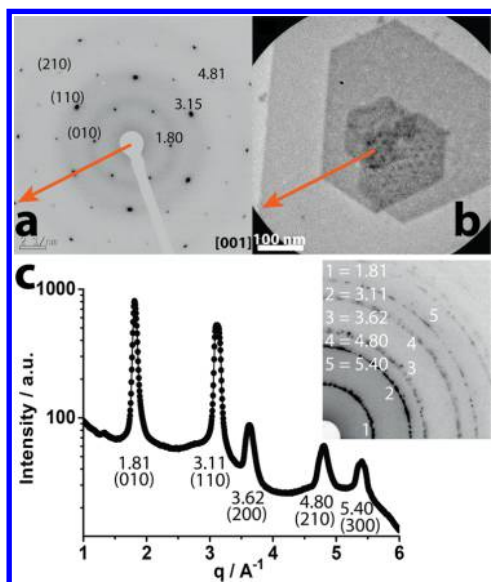


Figure 6. Crystallography of ultrathin InSe nanosheets. (a) ED of a single-crystalline sheet with (b) several terraces depicted in the bright-field TEM micrograph, all numbers are measured q -values in units of \AA^{-1} and all indices are based on a [001]-projection of a hexagonal unit cell with space group 194. The arrow indicates preferred direction of crystal growth, which is identified as the [110]-direction, (c) rotational scan intensity profile of the ED (inset) of a large ensemble of InSe nanosheets, the first five reflections are numbered, their q -values displayed in \AA^{-1} and assignable to hexagonal stoichiometric InSe (JCPDS file 01-075-1008).

nanocrystals. For further TEM characterization, the reader is referred to Figure S2. We chose to terminate the reaction for InSe nanosheets after 60 min at 240 °C to obtain the most stable synthesis product for the materials' properties characterization.

Thickness of Ultrathin InSe Nanosheets. AFM characterizes the total thickness of ultrathin InSe layers. GISAXS is used as complementary method for addressing the nanosheet

thickness and additionally constitutes the lamellar structure of the ligand template separating single inorganic InSe nanosheets. Figure 3a depicts height profiles of single InSe nanosheets with different lateral lengths. All nanosheets exhibit the same median total thickness of 5 nm (inorganic material layer and one organic ODA layer per front and backside of a sheet). Figure 3b shows the comparison of a single InSe nanosheet with a layer stack. A typical stack consists of four InSe layers with a height of four single InSe nanosheets (~ 22.5 nm).

For GISAXS analysis, we apply the model of a self-assembled lamellar ODA ligand separating single InSe sheets with long-range order on a large scale. The inorganic intersheet distance is fitted with a lamellar structure factor, representing the ordering of the ODA ligands on the sheet surface. Figure 4a shows the 2D pattern of InSe nanosheets lying flat on the surface with virtually only scattering in q_z -direction and no long-range ordering in q_y -direction. Figure 4b depicts a 1D scattering curve of InSe nanosheets at an incidence angle of 0.3° with an overall repetition, hence total thickness of the InSe sheets in their lamellar ODA template, of 4.4 nm (± 0.1 nm). The AFM (5 nm) and GISAXS (4.4 ± 0.1 nm) determined thickness of InSe sheets are thus in very good agreement. The slight disparity of the values arises from the fact that the sheet thickness determination by AFM has been performed on 50 single sheets, while GISAXS analysis averages over a macroscopic amount of InSe sheet stacks in the deposited sample. These stacks can exhibit reduced thickness, as ODA molecules between two sheets can interdigitate, leading to a reduced thickness measured for several stacked sheets. Additionally, a reduced ODA molecule monolayer length can also originate from a certain tilt of the surface-bound molecule as described by Oviedo et al.⁴⁹ They find a maximum shortened ODA molecule length of 1.7 nm in comparison to the full molecular length of ~ 2.5 nm, when ODA undergoes self-assembly on a substrate/surface. This description might also hold for ODA molecules stabilizing the InSe sheets.

XRDs of macroscopic InSe nanosheet samples additionally show a series of sharp reflections in the range of $0.2 \text{ \AA}^{-1} < q < 2.2 \text{ \AA}^{-1}$ (see Figures S3 and S4 with 2θ values converted to q -values for comparability). A number of these reflections are separated by multiples of $\Delta q = 0.139 (\pm 0.003) \text{ \AA}^{-1}$, hence 4.5 (± 0.1) nm and render the periodicity of InSe nanosheets in their ODA ligand template in striking similarity to the GISAXS analysis discussed above.

Knowing the total periodicity/thickness of 4.4–5 nm of ultrathin InSe nanosheets from AFM, GISAXS, and XRD, we can determine a minimum thickness of the inorganic InSe layer of only one InSe motif (0.84 nm) in the case of strongly interdigitating and/or fully tilted ODA molecules and a maximum thickness of the inorganic layer of one hexagonal unit cell (1.69 nm) in case of reduced interdigitating/tilting of ODA molecules.

Stoichiometry and Hexagonal Crystal Structure of Ultrathin InSe Nanosheets. The chemical composition of the InSe nanosheets is determined by X-ray photoelectron spectroscopy (XPS, Figure 5). To fit the raw data for the In(3d) and Se(3d) spectral regions, we use three constraints: A fixed In $3d_{5/2}$:In $3d_{3/2}$ as well as Se $3d_{5/2}$:Se $3d_{3/2}$ ratio of 3:2, a constant spin–orbit split for the two indium and selenium components and a fixed full-width at half-maximum (fwhm) for each element. We observe two In(3d) species with spin–orbit split doublets ($\Delta E = 7.6$ eV) at 444.8/452.4 eV and 445.8/453.4 eV, respectively (Figure 5a). Similarly, we detect two

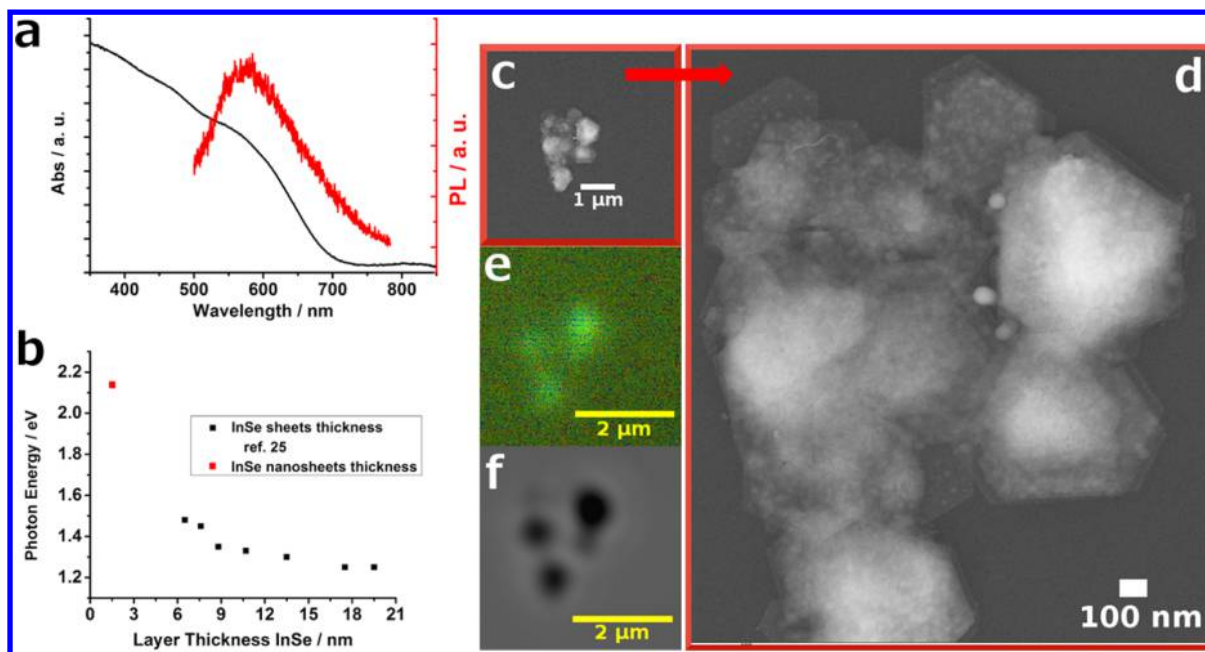


Figure 7. (a) Absorption of InSe nanosheets (in solution) at 560 nm (~ 2.2 eV) and broad PL at 580 nm (drop-casted), (b) comparison of band gap values depending on the sheet thickness of exfoliated InSe (data from ref 25) with the band gap of ultrathin InSe nanosheets from our colloidal approach, (c) SEM image of InSe sheets for confocal microscope PL measurements, (d) high magnification of image c, depicting InSe nanosheets stacks of different height, (e) PL shown by multiple InSe nanosheet stacks depicted in c–f, (f) image of InSe sheets in transmission mode of the confocal microscope.

Se(3d) species at 54.0/54.9 eV and 55.0/55.9 eV ($\Delta E = 0.9$ eV) which are typical values for metal selenides (Figure 5b). We find no signs of any Se–O bonds (~ 59 eV) in all samples. The O(1s) region exhibits a rather unspecific broad peak with a binding energy maximum at 533.1 eV. Owing to the history of the samples, this feature originates most likely from adsorbed oxygen/moisture and/or from the 2-propanol utilized during purification of the material after synthesis. We note that for (partially) oxidized indium, two O 1s signals are expected at roughly 530 and 532 eV, and that our O 1s spectrum does not show a significant shoulder in this region.^{26,50}

To determine the In:Se ratio from XPS, we use

$$C_{\text{In}}/C_{\text{Se}} = \frac{I_{\text{In}}/J_{\text{In}}}{F_{\text{In}}} / \frac{I_{\text{Se}}/J_{\text{Se}}}{F_{\text{Se}}}$$

where C_i is the concentration of the photoelectron emitting atom/ion within the sampled volume, J_i represents the X-ray flux striking the analyzed area, and F_i is the sensitivity factor of element i , given by

$$F_i = \alpha_{\text{pc}(i)} k_f \lambda_{\text{IMFP}(i)}$$

with $\alpha_{\text{pc}(i)}$ the photoelectron cross section of i , k_f the combined instrument factor, and $\lambda_{\text{IMFP}(i)}$ the inelastic mean free path (IMFP) of the photoelectron emitted by the element i . By keeping $J_{\text{In}} = J_{\text{Se}}$, the stoichiometric ratio In:Se of a typical nanosheet is directly inferred from the absolute areas of the fitted components. We find an average element In:Se ratio in the nanosheets of $1.1(\pm 0.1):1$. In light of the two different In and Se species, we attempt an analysis by postulating a mixture of two In_xSe_y species and compare both “low binding energy” as well as “high binding energy” In and Se components with each other. We note that in both cases, the overall 1.1:1 In:Se ratio is exactly obeyed. The component at lower binding energy is by far the most abundant with a relative content of

93.5%. Additionally, the In($3d_{5/2}$) (444.8 eV vs 444.7 eV) and Se($3d_{5/2}$) (54.0 eV vs 54.1 eV) signals are in rather good agreement with previous XPS investigations of InSe thin films.⁵¹ The same authors of this previous work report that freshly cleaved InSe single crystals without any surface-oxygen exhibit high In($3d_{5/2}$) and Se($3d_{5/2}$) binding energies of 445.7 and 55.1 eV, respectively, which are again in excellent agreement with our “high binding energy” component. The differences in binding energy of 1.0 eV between freshly cleaved and thin-film InSe are explained with surface modifications because of the exposure to ambient conditions by the authors, and we hold a similar effect responsible for the almost identical XPS data obtained with the material presented here.

To summarize the XPS experiment, our data suggest a near-stoichiometric indiumselenide composition with clear signs of surface modification (e.g., by organic surfactants). A minor portion (6.5%) is consistent with atomically clean InSe (e.g., atoms in the interior of a sheet).

Energy-dispersive X-ray spectroscopy (EDS) of InSe nanosheets provided ambiguous results for the sheets’ composition (see Figure S5). EDS showed an In:Se ratio of 1:1.8 which is an unknown stoichiometry in the InSe crystal structure and phase diagram.¹⁷ The stoichiometric composition of InSe nanosheets determined by XPS however, excellently corresponds with the crystallographic characterization of ultrathin InSe nanosheets (see Figure 6). Our analysis is carried out on a single crystalline sheet (Figure 6a, b) and on a larger ensemble of sheets including some smaller debris-like particles (Figure 6c and Figure S6). The electron diffraction (ED) shows a single-crystalline pattern, which can be indexed according to the [001] zone axis of a hexagonal unit cell. We find q -values (and their higher orders) of 1.80, 3.15, and 4.81 \AA^{-1} , which are identified as the (010), (110), and (210) reflection (see Figure 6a). These values are in excellent agreement with the hexagonal phase of stoichiometric InSe and space group 194 (JCPDS file 01–075–

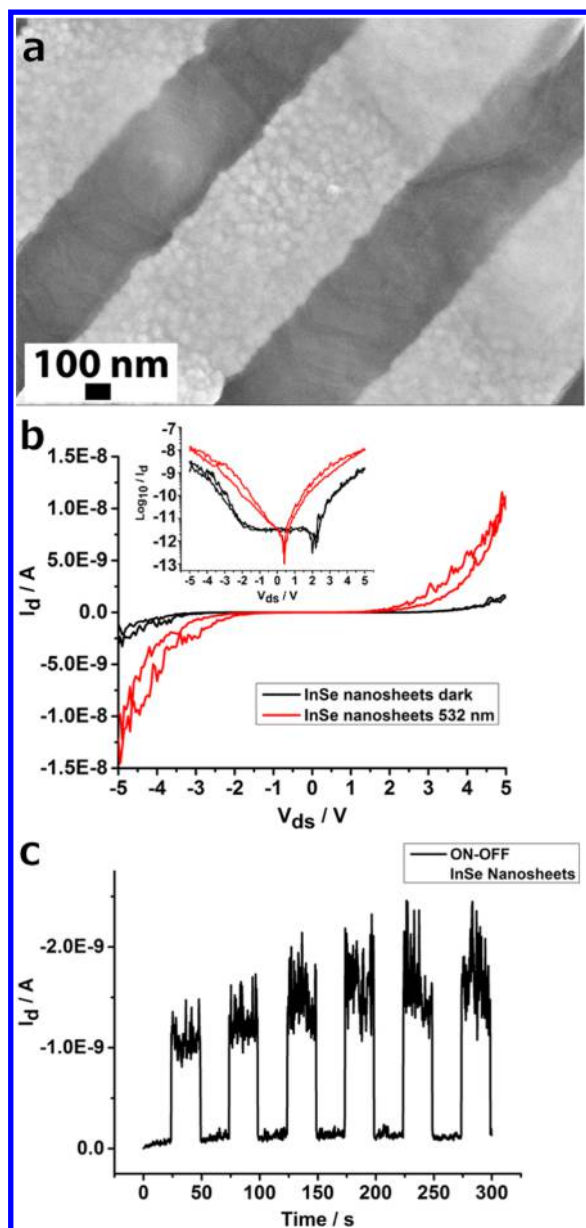


Figure 8. (a) InSe nanosheets, spin-coated onto 450 nm spaced gold electrodes, (b) output characteristics of InSe devices as shown in panel a, with 10-fold current increase under illumination, inset displaying semilogarithmic plot with suppressed current at a lateral bias voltage of ± 2 V due to contact barriers to be overcome by charge carriers as discussed in the main part, (c) reproducible on–off switching of the device.

1008). By comparing ED with the corresponding bright-field TEM micrograph, we reveal that growth occurs predominantly along the [110]-directions (indicated by the red arrows in Figure 6a, b). We note that the apparent terraces in Figure 6b (which should be compared to Figure 3a) do not affect the single-crystalline nature of the sheet.

Our conclusion of a stoichiometric composition and hexagonal structure of the InSe nanosheets presented here is underpinned by the rotational scan intensity profile of an ED of a large ensemble of such crystals (Figure 6c and Figure S6 for bright-field TEM micrograph). We clearly observe the (010), (110), (200), (210) and (300) reflections of hexagonal InSe (JCPDS file 01–075–1008) in the large ensemble.

Absorption and Photoluminescence of Ultrathin InSe Nanosheets.

InSe nanosheets exhibit a broad absorption feature near 560 nm (~ 2.2 eV, Figure 7a) and a broad emission at 580 nm (Figure 7a, 500 nm long pass filter used to cutoff 470 nm excitation wavelength). The distinct blue shift to higher energies in the absorption of InSe nanosheets as compared to thicker, exfoliated InSe and bulk sample values of 1.24 eV⁵² (Figure 7b, exfoliated InSe layer band gap values from ref 25, plotted for comparison) is attributed to the increasing binding energy of charge carriers in ultrathin InSe layers.^{24,52–54} A Bohr-exciton radius of 8.6 nm further leads to the appearance of strong quantum confinement effects in 2D InSe layers in the z-direction. In good agreement with results described by Mudd et al., the broad emission of InSe nanosheets can originate from dopant impurities exhibiting an increased binding energy in ultrathin InSe layers associated with a spectral broadening.²⁴ Up to now, photoluminescence (PL) of single ultrathin InSe nanosheets has not been shown, but we clearly detect a locally resolved PL signal originating from the InSe nanosheets (Figure 7d, e). Generally, the PL of InSe decreases with layer thickness²⁵ and can complicate detection of PL in single nanosheets because of the arising of a slightly indirect band gap in ultrathin InSe layers. A delocalized electronic state leads to a decrease of the indirect band gap transition in the InSe band structure slightly below the energy of the direct band gap transition (as described for 2D InSe nanocrystals²³ and for InSe sheets with a thickness of ≤ 7 atomic layers¹⁴). The low PL of ultrathin InSe nanosheets might also originate from increasing localized trap states in thin layers, leading to only weakly emitting InSe sheets.

Electrical Transport in Ultrathin InSe Nanosheets. We probed the current–voltage characteristics of the pristine nanosheets (with ligands) to monitor their potential for photodetection, and find promising reproducible on–off switching under illumination. After drop-casting InSe nanosheets onto interdigitating gold electrodes with 450 nm spacing (Figure 8a and Figure S7 for devices), electrical transport measurements on sheet ensembles are carried out at room temperature under vacuum in the dark and under illumination at 532 nm using a laser diode (13.2 mW/cm²). Figure 8b displays current–voltage outputs of InSe devices, the inset showing the same data on a semilogarithmic scale. A suppressed current at a lateral bias voltage of ± 2 V indicates a contact barrier for charge carriers to overcome (Figure 8b, inset). However, when illuminated, InSe devices exhibit a substantial current increase by the factor 10 for an intensity of 13.2 mW/cm² ($V_{ds} = 5$ V, $V_g = 0$ V, Figure 8b). As InSe sheet ensembles are randomly distributed on the gold electrodes, charge carriers have to pass multiple contact barriers between single sheets and at the electrodes to be collected. Improving the contacts (e.g., different metal electrodes and direct contacting of InSe sheets) is therefore currently investigated. Figure 8c shows that despite of the nonideal contacting InSe devices exhibit considerable dynamic photoresponse when switched on and off.

CONCLUSION

We demonstrate a solution-processable pathway to 2D InSe with an ultrathin inorganic layer thickness of minimum one InSe motif (0.84 nm) to maximum one unit cell (1.69 nm) and lateral sizes up to 800 nm. The comprehensive crystallographic, compositional and microscopic analysis of the nanosheets reveals the formation of a stoichiometric hexagonal InSe phase

by the connection of an inorganic InSe core with an organic amine-based crystalline template. Absorption and locally resolved confocal photoluminescence measurements additionally prove the strong quantum confinement of 2D InSe layers in the *z*-direction. Under photoexcitation, these ultrathin InSe nanosheets exhibit a 10-fold current increase and reproducible on and off switching of the device. The colloidal ligand template method to 2D materials presented here yields crystal thicknesses, which are hardly accessible by exfoliation techniques and represents a strong addition for synthesizing and hence accessing more functional 2D materials for ultrathin electronics.

■ ASSOCIATED CONTENT

Supporting Information

The Supporting Information is available free of charge on the ACS Publications website at DOI: [10.1021/acs.chemmater.5b04646](https://doi.org/10.1021/acs.chemmater.5b04646).

Additional TEM and SEM images, EDS and XRD data (PDF)

■ AUTHOR INFORMATION

Corresponding Author

*E-mail: j.d.lauth@tudelft.nl.

Author Contributions

[†]J.L. and F.E.S.G. contributed equally to this work. The manuscript was written through contributions of all authors. All authors have given approval to the final version of the manuscript.

Funding

J.L. gratefully acknowledges a Pro Exzellenzia Postdoctoral fellowship. F.E.S.G. gratefully acknowledges a University of Hamburg doctoral fellowship. C. K. thanks the German Research Foundation (DFG) for granting the project KL 1453/9-1 and the European Research Council for funding an ERC Starting Grant (Project: 2D-SYNETRA (304980)), Seventh Framework Program FP7). V. L. is grateful to the DFG for financial support in the frame of the Cluster of Excellence "Center of Ultrafast Imaging CUI". Financial support of M. S. K. and M. S. has been provided in equal parts by the Institutional Strategy of the University of Tuebingen (DFG, ZUK 63) and the Baden-Württemberg Stiftung by the Eliteprogram for Postdocs.

Notes

The authors declare no competing financial interest.

■ ACKNOWLEDGMENTS

A. Hirsch from the Alf Mews group is gratefully acknowledged for performing the InSe nanosheet fluorescence measurement on the drop-casted sample together with W. Friedrich.

■ REFERENCES

- (1) Wang, Q. H.; Kalantar-Zadeh, K.; Kis, A.; Coleman, J. N.; Strano, M. S. Electronics and Optoelectronics of Two-Dimensional Transition Metal Dichalcogenides. *Nat. Nanotechnol.* **2012**, *7*, 699–712.
- (2) Butler, S. Z.; Hollen, S. M.; Cao, L.; Cui, Y.; Gupta, J. A.; Gutiérrez, H. R.; Heinz, T. F.; Hong, S. S.; Huang, J.; Ismach, A. F.; et al. Progress, Challenges, and Opportunities in Two-Dimensional Materials Beyond Graphene. *ACS Nano* **2013**, *7*, 2898–2926.
- (3) Huang, X.; Zeng, Z.; Zhang, H. Metal Dichalcogenide Nanosheets: Preparation, Properties and Applications. *Chem. Soc. Rev.* **2013**, *42*, 1934–1946.

- (4) Kumar, A.; Ahluwalia, P. K. Electronic Structure of Transition Metal Dichalcogenides Monolayers 1H-MX₂ (M = Mo, W; X = S, Se, Te) from Ab-Initio Theory: New Direct Band Gap Semiconductors. *Eur. Phys. J. B* **2012**, *85*, 1–7.

- (5) Lim, H.; Yoon, S. I.; Kim, G.; Jang, A.-R.; Shin, H. S. Stacking of Two-Dimensional Materials in Lateral and Vertical Directions. *Chem. Mater.* **2014**, *26*, 4891–4903.

- (6) Lopez-Sanchez, O.; Lembke, D.; Kayci, M.; Radenovic, A.; Kis, A. Ultrasensitive Photodetectors Based on Monolayer MoS₂. *Nat. Nanotechnol.* **2013**, *8*, 497–501.

- (7) Mas-Balleste, R.; Gomez-Navarro, C.; Gomez-Herrero, J.; Zamora, F. 2D Materials: To Graphene and Beyond. *Nanoscale* **2011**, *3*, 20–30.

- (8) Radisavljevic, B.; Radenovic, A.; Brivio, J.; Giacometti, V.; Kis, A. Single-Layer MoS₂ Transistors. *Nat. Nanotechnol.* **2011**, *6*, 147–150.

- (9) Sun, Z.; Chang, H. Graphene and Graphene-like Two-Dimensional Materials in Photodetection: Mechanisms and Methodology. *ACS Nano* **2014**, *8*, 4133–4156.

- (10) Lei, S.; Wen, F.; Li, B.; Wang, Q.; Huang, Y.; Gong, Y.; He, Y.; Dong, P.; Bellah, J.; George, A.; et al. Optoelectronic Memory Using Two-Dimensional Materials. *Nano Lett.* **2015**, *15*, 259–265.

- (11) Sucharitakul, S.; Goble, N. J.; Kumar, U. R.; Sankar, R.; Bogorad, Z. A.; Chou, F.-C.; Chen, Y.-T.; Gao, X. P. A. Intrinsic Electron Mobility Exceeding 10³ cm²/(Vs) in Multilayer InSe FETs. *Nano Lett.* **2015**, *15*, 3815.

- (12) Feng, W.; Zheng, W.; Cao, W.; Hu, P. Back Gated Multilayer InSe Transistors with Enhanced Carrier Mobilities via the Suppression of Carrier Scattering from a Dielectric Interface. *Adv. Mater.* **2014**, *26*, 6587–6593.

- (13) Tamalampudi, S. R.; Lu, Y.-Y.; Kumar, U. R.; Sankar, R.; Liao, C.-D.; Moorthy, B., K.; Cheng, C.-H.; Chou, F. C.; Chen, Y.-T. High Performance and Bendable Few-Layered InSe Photodetectors with Broad Spectral Response. *Nano Lett.* **2014**, *14*, 2800–2806.

- (14) Lei, S.; Ge, L.; Najmaei, S.; George, A.; Kappera, R.; Lou, J.; Chhowalla, M.; Yamaguchi, H.; Gupta, G.; Vajtai, R.; et al. Evolution of the Electronic Band Structure and Efficient Photo-Detection in Atomic Layers of InSe. *ACS Nano* **2014**, *8*, 1263–1272.

- (15) Lei, S.; Wen, F.; Ge, L.; Najmaei, S.; George, A.; Gong, Y.; Gao, W.; Jin, Z.; Li, B.; Lou, J.; et al. An Atomically Layered InSe Avalanche Photodetector. *Nano Lett.* **2015**, *15*, 3048–3055.

- (16) Debbichi, L.; Eriksson, O.; Lebègue, S. Two-Dimensional Indium Selenides Compounds: An Ab Initio Study. *J. Phys. Chem. Lett.* **2015**, *6*, 3098–3103.

- (17) Okamoto, H. In-Se (Indium-Selenium). *J. Phase Equilib. Diffus.* **2004**, *25*, 201–201.

- (18) Imai, K.; Suzuki, K.; Haga, T.; Hasegawa, Y.; Abe, Y. Phase Diagram of Indium-Selenide System and Crystal Growth of Indium Monoselenide. *J. Cryst. Growth* **1981**, *54*, 501–506.

- (19) Hergert, F.; Jost, S.; Hock, R.; Purwins, M. A Crystallographic Description of Experimentally Identified Formation Reactions of Cu(In,Ga)Se₂. *J. Solid State Chem.* **2006**, *179*, 2394–2415.

- (20) Klemm, W.; van Vogel, H. U. Messungen an Gallium- und Indium-Verbindungen. X. Über die Chalkogenide von Gallium und Indium. *Z. Anorg. Allg. Chem.* **1934**, *219*, 45–64.

- (21) Splendiani, A.; Sun, L.; Zhang, Y.; Li, T.; Kim, J.; Chim, C.-Y.; Galli, G.; Wang, F. Emerging Photoluminescence in Monolayer MoS₂. *Nano Lett.* **2010**, *10*, 1271–1275.

- (22) Yang, S.; Kelley, D. F. Transient Absorption Spectra and Dynamics of InSe Nanoparticles. *J. Phys. Chem. B* **2006**, *110*, 13430–13435.

- (23) Yang, S.; Kelley, D. F. The Spectroscopy of InSe Nanoparticles. *J. Phys. Chem. B* **2005**, *109*, 12701–12709.

- (24) Mudd, G. W.; Patanè, A.; Kudrynskiy, Z. R.; Fay, M. W.; Makarovskiy, O.; Eaves, L.; Kovalyuk, Z. D.; Zólyomi, V.; Falko, V. Quantum Confined Acceptors and Donors in InSe Nanosheets. In *Appl. Phys. Lett.*, **2014**; Vol. 105, pp 221909–5.10.1063/1.4903738

- (25) Mudd, G. W.; Svatek, S. A.; Ren, T.; Patanè, A.; Makarovskiy, O.; Eaves, L.; Beton, P. H.; Kovalyuk, Z. D.; Lashkarev, G. V.; Kudrynskiy,

Z. R.; et al. Tuning the Bandgap of Exfoliated InSe Nanosheets by Quantum Confinement. *Adv. Mater.* **2013**, *25*, 5714–5718.

(26) Ho, C.-H.; Lin, C.-H.; Wang, Y.-P.; Chen, Y.-C.; Chen, S.-H.; Huang, Y.-S. Surface Oxide Effect on Optical Sensing and Photoelectric Conversion of α -In₂Se₃ Hexagonal Microplates. *ACS Appl. Mater. Interfaces* **2013**, *5*, 2269–2277.

(27) Wu, D.; Pak, A. J.; Liu, Y.; Zhou, Y.; Wu, X.; Zhu, Y.; Lin, M.; Han, Y.; Ren, Y.; Peng, H.; et al. Thickness-Dependent Dielectric Constant of Few-Layer In₂Se₃ Nanoflakes. *Nano Lett.* **2015**, *15*, 8136–8140.

(28) Lin, M.; Wu, D.; Zhou, Y.; Huang, W.; Jiang, W.; Zheng, W.; Zhao, S.; Jin, C.; Guo, Y.; Peng, H.; et al. Controlled Growth of Atomically Thin In₂Se₃ Flakes by van der Waals Epitaxy. *J. Am. Chem. Soc.* **2013**, *135*, 13274–13277.

(29) Schliehe, C.; Juarez, B. H.; Pelletier, M.; Jander, S.; Greshnykh, D.; Nagel, M.; Meyer, A.; Foerster, S.; Kornowski, A.; Klinke, C.; et al. Ultrathin PbS Sheets by Two-Dimensional Oriented Attachment. *Science* **2010**, *329*, 550–553.

(30) Wang, F.; Wang, Y.; Liu, Y.-H.; Morrison, P. J.; Loomis, R. A.; Buhro, W. E. Two-Dimensional Semiconductor Nanocrystals: Properties, Templated Formation, and Magic-Size Nanocluster Intermediates. *Acc. Chem. Res.* **2015**, *48*, 13–21.

(31) Bouet, C.; Mahler, B.; Nadal, B.; Abecassis, B.; Tessier, M. D.; Ithurria, S.; Xu, X.; Dubertret, B. Two-Dimensional Growth of CdSe Nanocrystals, from Nanoplatelets to Nanosheets. *Chem. Mater.* **2013**, *25*, 639–645.

(32) Lhuillier, E.; Pedetti, S.; Ithurria, S.; Nadal, B.; Heuclin, H.; Dubertret, B. Two-Dimensional Colloidal Metal Chalcogenides Semiconductors: Synthesis, Spectroscopy, and Applications. *Acc. Chem. Res.* **2015**, *48*, 22–30.

(33) Son, J. S.; Wen, X.-D.; Joo, J.; Chae, J.; Baek, S.-i.; Park, K.; Kim, J. H.; An, K.; Yu, J. H.; Kwon, S. G.; et al. Large-Scale Soft Colloidal Template Synthesis of 1.4 nm Thick CdSe Nanosheets. *Angew. Chem., Int. Ed.* **2009**, *48*, 6861–6864.

(34) Son, J. S.; Yu, J. H.; Kwon, S. G.; Lee, J.; Joo, J.; Hyeon, T. Colloidal Synthesis of Ultrathin Two-Dimensional Semiconductor Nanocrystals. *Adv. Mater.* **2011**, *23*, 3214–3219.

(35) Han, J. H.; Lee, S.; Cheon, J. Synthesis and Structural Transformations of Colloidal 2D Layered Metal Chalcogenide Nanocrystals. *Chem. Soc. Rev.* **2013**, *42*, 2581–2591.

(36) Wang, Z.; Schliehe, C.; Wang, T.; Nagaoka, Y.; Cao, Y. C.; Bassett, W. A.; Wu, H.; Fan, H.; Weller, H. Deviatoric Stress Driven Formation of Large Single-Crystal PbS Nanosheet from Nanoparticles and in Situ Monitoring of Oriented Attachment. *J. Am. Chem. Soc.* **2011**, *133*, 14484–14487.

(37) Joo, J.; Son, J. S.; Kwon, S. G.; Yu, J. H.; Hyeon, T. Low-Temperature Solution-Phase Synthesis of Quantum Well Structured CdSe Nanoribbons. *J. Am. Chem. Soc.* **2006**, *128*, 5632–5633.

(38) Liu, Y.-H.; Wang, F.; Wang, Y.; Gibbons, P. C.; Buhro, W. E. Lamellar Assembly of Cadmium Selenide Nanoclusters into Quantum Belts. *J. Am. Chem. Soc.* **2011**, *133*, 17005–17013.

(39) Wang, Y.; Liu, Y.-H.; Zhang, Y.; Kowalski, P. J.; Rohrs, H. W.; Buhro, W. E. Preparation of Primary Amine Derivatives of the Magic-Size Nanocluster (CdSe)₁₃. *Inorg. Chem.* **2013**, *52*, 2933–2938.

(40) Wang, Y.; Zhang, Y.; Wang, F.; Giblin, D. E.; Hoy, J.; Rohrs, H. W.; Loomis, R. A.; Buhro, W. E. The Magic-Size Nanocluster (CdSe)₃₄ as a Low-Temperature Nucleant for Cadmium Selenide Nanocrystals; Room-Temperature Growth of Crystalline Quantum Platelets. *Chem. Mater.* **2014**, *26*, 2233–2243.

(41) Wang, Y.; Zhou, Y.; Zhang, Y.; Buhro, W. E. Magic-Size II–VI Nanoclusters as Synthons for Flat Colloidal Nanocrystals. *Inorg. Chem.* **2015**, *54*, 1165–1177.

(42) Morrison, P. J.; Loomis, R. A.; Buhro, W. E. Synthesis and Growth Mechanism of Lead Sulfide Quantum Platelets in Lamellar Mesophase Templates. *Chem. Mater.* **2014**, *26*, 5012–5019.

(43) Du, Y.; Yin, Z.; Zhu, J.; Huang, X.; Wu, X.-J.; Zeng, Z.; Yan, Q.; Zhang, H. A General Method for the Large-scale Synthesis of Uniform Ultrathin Metal Sulphide Nanocrystals. *Nat. Commun.* **2012**, *3*, 1177.

(44) Park, K. H.; Jang, K.; Kim, S.; Kim, H. J.; Son, S. U. Phase-Controlled One-Dimensional Shape Evolution of InSe Nanocrystals. *J. Am. Chem. Soc.* **2006**, *128*, 14780–14781.

(45) Airo, M. A.; Gqoba, S.; Kalenga, M. P.; Govindraj, S.; Moloto, M. J.; Moloto, N. Synthesis and Characterization of Indium Monoselenide Nanosheets: A Proposed Pseudo Top-Down Mechanism. *J. Cryst. Growth* **2014**, *406*, 1–7.

(46) Förster, S.; Apostol, L.; Bras, W. Scatter: Software for the Analysis of Nano- and Mesoscale Small-Angle Scattering. *J. Appl. Crystallogr.* **2010**, *43*, 639–646.

(47) Förster, S.; Timmann, A.; Konrad, M.; Schellbach, C.; Meyer, A.; Funari, S. S.; Mulvaney, P.; Knott, R. Scattering Curves of Ordered Mesoscopic Materials. *J. Phys. Chem. B* **2005**, *109*, 1347–1360.

(48) Bullen, C.; van Embden, J.; Jasieniak, J.; Cosgriff, J. E.; Mulder, R. J.; Rizzardo, E.; Gu, M.; Raston, C. L. High Activity Phosphine-Free Selenium Precursor Solution for Semiconductor Nanocrystal Growth. *Chem. Mater.* **2010**, *22*, 4135–4143.

(49) Oviedo, J.; San-Miguel, M. A.; Heredia-Guerrero, J. A.; Benítez, J. J. Electrostatic Induced Molecular Tilting in Self-Assembled Monolayers of n-Octadecylamine on Mica. *J. Phys. Chem. C* **2012**, *116*, 7099–7105.

(50) Faur, M.; Faur, M.; Jayne, D. T.; Goradia, M.; Goradia, C. XPS Investigation of Anodic Oxides Grown on p-type InP. *Surf. Interface Anal.* **1990**, *15*, 641–650.

(51) Brojerdi, G.; Tyuliev, G.; Fargues, D.; Eddrief, M.; Balkanski, M. Ion Beam Modification of InSe Surfaces. *Surf. Interface Anal.* **1997**, *25*, 111–118.

(52) Madelung, O. *Semiconductors: Data Handbook*. 3 ed.; Springer: London, 2003.

(53) Yoffe, A. D. Low-Dimensional Systems: Quantum Size Effects and Electronic Properties of Semiconductor Microcrystallites (Zero-Dimensional Systems) and some Quasi-Two-Dimensional Systems. *Adv. Phys.* **1993**, *42*, 173–262.

(54) Yoffe, A. D. Layer Compounds. *Annu. Rev. Mater. Sci.* **1973**, *3*, 147–170.